

# Motif-Based Design for Connected Vehicle Systems in Presence of Heterogeneous Connectivity Structures and Time Delays

Linjun Zhang and Gábor Orosz

**Abstract**—In this paper, we investigate the effects of heterogeneous connectivity structures and information delays on the dynamics of connected vehicle systems (CVSs), which are composed of vehicles equipped with connected cruise control (CCC) as well as conventional vehicles. First, a general framework is presented for CCC design that incorporates information delays and allows a large variety of connectivity structures. Then, we present delay-dependent criteria for plant stability and head-to-tail string stability of CVSs. The stability conditions are visualized by using stability diagrams, which allow one to evaluate the robustness of vehicle networks against information delays. To achieve modular and scalable design of large networks, we also propose a motif-based approach. Our results demonstrate the advantages of CCC vehicles in improving traffic efficiency, but also show that increasing the penetration of CCC vehicles does not necessarily improve the robustness if the connectivity structure or the control gains are not appropriately designed.

**Index Terms**—Wireless vehicle-to-vehicle (V2V) communication, connected cruise control, time delay, stability.

## I. INTRODUCTION

IN conventional traffic, each vehicle responds to the motion of vehicles within the line of sight, typically just the vehicle immediately ahead [1]–[3]. However, by using wireless vehicle-to-vehicle (V2V) communication, one may obtain information about distant vehicles beyond the line of sight, which has great potential for enhancing safety of vehicles [4], [5], improving traffic efficiency [6]–[8], and reducing fuel consumption [9]. A typical application of V2V communication is cooperative adaptive cruise control (CACC), where a platoon of vehicles are connected such that each vehicle responds to the motion of the vehicle immediately ahead by using adaptive cruise control (ACC), while they also monitor the motion of a designated platoon leader via V2V communication [10]. Studies in [11]–[15] have shown the advantage of CACC in improving traffic flow by attenuating disturbances. However,

CACC requires that multiple ACC vehicles travel next to each other, which rarely occurs in practice due to the low penetration of such vehicles. Moreover, CACC relies on a designated platoon leader and a predetermined connectivity structure.

To relax the aforementioned limitations, we put forward the concept of connected cruise control (CCC), which utilizes the information received from multiple vehicles ahead by exploiting the ad-hoc nature of V2V communication. CCC may be used either to assist human drivers or to automatically control vehicles based on communication and sensor information. The advantage of CCC in improving traffic efficiency have been studied in [16]–[18]. Motivated by the heterogeneity of real traffic, we also investigate connected vehicle systems (CVSs) where multiple CCC vehicles are mixed into the flow of human-driven vehicles and ACC vehicles. Compared with CACC platoons, CVSs are more flexible and scalable since they allow the incorporation of vehicles that are not equipped with range sensors or wireless transceivers. In addition, CVSs require neither a designated platoon leader nor a prescribed connectivity structure. However, the analysis and design of CVSs are challenging due to the complex connectivity structures in real traffic. Communication delays, which arise from intermittency and packet drops, lead to additional complexity.

In this paper, we establish the fundamental principles for evaluating the effects of connectivity structures and information delays on the dynamics of CVSs. First, we propose a general framework for CCC design that includes information delays and allows a large variety of connectivity structures. This framework ensures the existence of a unique equilibrium, which is independent of network size, connectivity structure, control gains, and information delays. Second, we propose a systematic method to calculate transfer functions of complicated networks in an efficient way, which is crucial for characterizing stability and disturbance attenuation of CVSs. Third, for a class of CVSs with repetitive structures, we provide a condition that ensures disturbance attenuation for large networks. Fourth, to achieve modular and scalable design of CVSs, we propose a motif-based approach which is inspired by recent results in systems biology [19]. The key idea is that vehicle networks can be constructed by combining fundamental motifs (simple networks that contain one CCC vehicle at the tail). By analyzing the dynamics of individual motifs and characterizing the effects of motif combinations, one can modularly construct vehicle networks that are robust against information delays and scalable for a large number of vehicles. To facilitate the design of

Manuscript received February 27, 2015; revised October 8, 2015; accepted December 10, 2015. Date of publication January 20, 2016; date of current version May 26, 2016. This work was supported by the National Science Foundation under Award 1351456. The Associate Editor for this paper was H. Julia.

The authors are with the Department of Mechanical Engineering, University of Michigan, Ann Arbor, MI 48109 USA (e-mail: linjunzh@umich.edu; orosz@umich.edu).

Color versions of one or more of the figures in this paper are available online at <http://ieeexplore.ieee.org>.

Digital Object Identifier 10.1109/TITS.2015.2509782

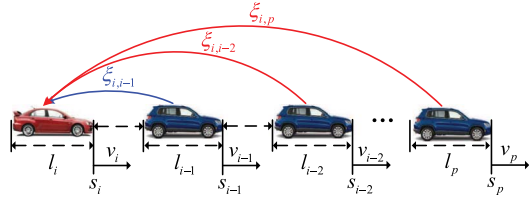


Fig. 1. Vehicle network where a CCC vehicle (red) receives information from multiple vehicles ahead. Arrows denote the directions of information flow. The blue link can be realized by human perception, range sensors or V2V communication, while the red links can only be realized by V2V communication. Symbols  $s_j$ ,  $l_j$ , and  $v_j$  denote the position, length, and velocity of vehicle  $j$ , respectively. Also,  $\xi_{i,j}$  denotes the delay of vehicle  $i$  receiving information from vehicle  $j$ .

CVSSs, the derived stability conditions are visualized in stability diagrams. Our results demonstrate the great potential of CCC vehicles in improving traffic efficiency, but also show that, for certain connectivity structures, increasing penetration of CCC vehicles may deteriorate network performance.

The rest of this paper is organized as follows. In Section II, a general framework is presented for CCC design in presence of heterogeneous connectivity structures and information delays. In Section III, we provide conditions for plant stability and head-to-tail string stability for general CVSSs. In Section IV and Section V, fundamental motifs and motif combinations are investigated, and the corresponding design principles are provided. Finally, we conclude our results in Section VI.

## II. DYNAMICS OF CONNECTED VEHICLE SYSTEMS

In this section, a general framework is presented for CCC design while considering heterogeneous connectivity structures and information delays. We use the phrase non-CCC to represent vehicles that are not equipped with CCC devices, although these vehicles may still broadcast their motion information. For CVSSs that consist of CCC and non-CCC vehicles, our design ensures the existence of a unique equilibrium, which is independent of the connectivity structure, network size, information delays, and control gains.

Fig. 1 shows a vehicle network where the CCC vehicle  $i$  monitors the positions and velocities of vehicles  $j = p, \dots, i-1$  where vehicle  $p$  is the furthest broadcasting vehicle within the effective communication range of vehicle  $i$ . Here,  $s_j$ ,  $v_j$ , and  $l_j$  denote the position, velocity, and length of vehicle  $j$ , respectively. Moreover,  $\xi_{i,j}$  denotes the information delay between vehicles  $j$  and  $i$ , which can be human reaction time, sensing delay, or communication delay. Note that communication delays are caused by intermittency and packet drops in V2V communication. Indeed, the motion of the vehicle immediately ahead can be monitored by human perception, range sensors (e.g., radar), or V2V communication, while the motion of distant vehicles can only be monitored by using V2V communication. Here, we assume that the CCC vehicle  $i$  can identify the number of vehicles between itself and vehicle  $k$  for  $k = i-1, \dots, p$  by using the position and velocity information received from vehicle  $k$ . In general, such identification is a challenging problem that is left for future research.

The connectivity structure of a network can be represented by using the adjacency matrix  $\Gamma = [\gamma_{i,j}]$  defined by

$$\gamma_{i,j} = \begin{cases} 1, & \text{if vehicle } i \text{ utilizes data of vehicle } j \\ 0, & \text{otherwise.} \end{cases} \quad (1)$$

We assume that each vehicle only responds to the motion of vehicles ahead, so information only propagates upstream. Correspondingly, we have  $\gamma_{i,j} = 0$  for  $i \leq j$ , and thus,  $\Gamma$  is a lower triangular matrix.

In this paper, we neglect the air-drag and the rolling resistance in the physics-based model [20], [21]. Thus, the acceleration of vehicle  $i$  is directly determined by the controller. Incorporating the data received from vehicles ahead, we design the longitudinal dynamics of the CCC vehicle  $i$  as

$$\begin{aligned} \dot{s}_i(t) &= v_i(t) \\ \dot{v}_i(t) &= \sum_{j=p}^{i-1} \gamma_{i,j} [\alpha_{i,j} (V_i(h_{i,j}(t - \xi_{i,j})) - v_i(t - \xi_{i,j})) \\ &\quad + \beta_{i,j} (v_j(t - \xi_{i,j}) - v_i(t - \xi_{i,j}))] \end{aligned} \quad (2)$$

where the quantity

$$h_{i,j} = \frac{1}{i-j} \left( s_j - s_i - \sum_{k=j}^{i-1} l_k \right) \quad (3)$$

denotes the average headway between vehicles  $i$  and  $j$ . The controller ((2), (3)) is designed to maintain a velocity-dependent headway from the vehicle immediately ahead and to maintain  $k$  times of this headway from the vehicle that is  $k$  vehicles ahead. Meanwhile, the controller intends to match the speed of the host vehicle to the speed of vehicles ahead. The constant gain  $\alpha_{i,j}$  is used for the average headway  $h_{i,j}$  while the constant gain  $\beta_{i,j}$  is used for the relative speed between vehicle  $j$  and vehicle  $i$ .

The range policy  $V_i(h)$  gives the desired velocity as a function of the headway  $h$ . Based on human drivers [3], we assume the range policy in the form

$$V(h) = \begin{cases} 0, & \text{if } h \leq h_{st} \\ F(h), & \text{if } h_{st} < h < h_{go} \\ v_{max}, & \text{if } h \geq h_{go} \end{cases} \quad (4)$$

where the function  $F(h)$  is continuous and strictly monotonically increasing with  $F(h_{st}) = 0$  and  $F(h_{go}) = v_{max}$ . This means that for small headways  $h \leq h_{st}$ , the vehicle tends to stop for safety reasons. For large headways  $h \geq h_{go}$ , the vehicle aims to maintain the preset maximum velocity  $v_{max}$ . Between  $h_{st}$  and  $h_{go}$ , the desired velocity monotonically increases with the headway. The two possible choices

$$F(h) = v_{max} \frac{h - h_{st}}{h_{go} - h_{st}} \quad (5)$$

$$F(h) = \frac{v_{max}}{2} \left[ 1 - \cos \left( \frac{\pi(h - h_{st})}{h_{go} - h_{st}} \right) \right] \quad (6)$$

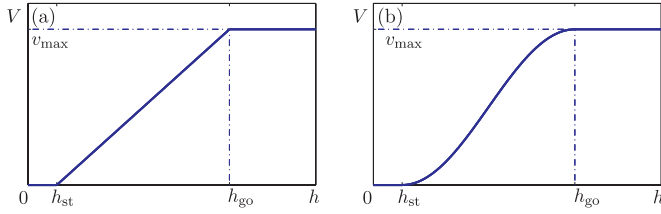


Fig. 2. Range policy functions defined by (4). Panels (a) and (b) correspond to formulae (5) and (6), respectively.

are shown in Fig. 2(a) and (b), respectively. The linear function (5) has discontinuities in the gradient at  $h = h_{st}$  and  $h = h_{go}$ , which leads to discontinuities in the jerk that may discomfort the driver. Thus, we use the nonlinear function (6) that results in smooth derivatives at  $h = h_{st}$  and  $h = h_{go}$ .

When all vehicles use the same range policy (i.e.,  $V_i(h) = V(h)$  for all  $i$ ), the framework (2) ensures the existence of so-called *uniform flow equilibrium*

$$s_i^*(t) = v^*t + s_i^0, \quad v_i(t) \equiv v^* \quad (7)$$

for all  $i$ , where  $s_i^0$  is a constant offset. Substituting (3) and (7) into (2) yields

$$h_{i,i-1}(t) \equiv s_{i-1}^0 - s_i^0 - l_{i-1} = h^*, \quad v^* = V(h^*) \quad (8)$$

for all  $i$ . In practice, range policies may differ for each vehicle in which case the equilibrium still exists but is not uniform. That is, (7) still holds but (8) is modified to  $h_{i,i-1}(t) \equiv h_{i,i-1}^*$  and  $v^* = V_i(h_{i,i-1}^*)$ , where  $h_{i,i-1}^*$  may be different for each vehicle. Since traffic data indicate that the equilibrium is typically close to uniform [3], we neglect such heterogeneities for simplicity. Throughout this paper, we use  $h_{st} = 5$  [m],  $h_{go} = 35$  [m], and  $v_{max} = 30$  [m/s] in the range policy (4).

*Remark:* In practice, the equilibrium of CVSs is determined by the velocity of the head vehicle, which may be not known in advance. For robustness, we consider the worst case scenario in terms of stability. Based on our observation, this corresponds to the equilibrium  $h^* = 20$  [m] and  $v^* = V(h^*) = 15$  [m/s], which results in  $V'(h^*) = \max\{V'(h)\} = \pi/2$  [1/s] corresponding to the smallest equilibrium time gap  $T_{gap} = 1/V'(h^*)$ .

The CCC framework ((2), (3)) ensures that the uniform flow equilibrium ((7), (8)) is unique and independent of network size, connectivity structures, information delays, and control gains. In this paper, we investigate the dynamics in the vicinity of the equilibrium and use the perturbations  $\tilde{s}_i(t) = s_i(t) - s_i^*(t)$  and  $\tilde{v}_i(t) = v_i(t) - v^*$  to describe the dynamics. To simplify expressions, we define the time shift operator

$$\mathcal{D}_\xi \chi(t) = \chi(t - \xi). \quad (9)$$

Hence, linearizing ((2), (3)) about the equilibrium ((7), (8)) leads to

$$\begin{aligned} \dot{\tilde{x}}_i(t) &= \mathbf{A}_0 \tilde{x}_i(t) + \sum_{j=p}^{i-1} \gamma_{i,j} \mathcal{D}_{\xi_{i,j}} (\mathbf{A}_{i,j} \tilde{x}_i(t) + \mathbf{B}_{i,j} \tilde{x}_j(t)) \\ \tilde{y}_i(t) &= \tilde{v}_i(t) = \mathbf{C} \tilde{x}_i(t) \end{aligned} \quad (10)$$

where  $\tilde{x}_i(t) = [\tilde{s}_i(t), \tilde{v}_i(t)]^T$  and the matrices are given by

$$\begin{aligned} \mathbf{A}_0 &= \begin{bmatrix} 0 & 1 \\ 0 & 0 \end{bmatrix}, \quad \mathbf{A}_{i,j} = \begin{bmatrix} 0 & 0 \\ -\varphi_{i,j} & -\kappa_{i,j} \end{bmatrix} \\ \mathbf{B}_{i,j} &= \begin{bmatrix} 0 & 0 \\ \varphi_{i,j} & \beta_{i,j} \end{bmatrix}, \quad \mathbf{C} = [0 \quad 1] \end{aligned} \quad (11)$$

$$\varphi_{i,j} = \frac{\alpha_{i,j} V'(h^*)}{i-j}, \quad \kappa_{i,j} = \alpha_{i,j} + \beta_{i,j}, \quad i > j. \quad (12)$$

The model (10)–(12) will be used in the rest of this paper to investigate the design of control gains  $\alpha_{i,j}$  and  $\beta_{i,j}$  for stability and disturbance attenuation along vehicle networks.

### III. PLANT STABILITY AND HEAD-TO-TAIL STRING STABILITY IN CONNECTED VEHICLE SYSTEMS

To characterize the system-level performance of CVSs, we investigate *plant stability* and *head-to-tail string stability*, which are defined as follow.

*Definition 1:* Plant stability indicates that the equilibrium of the CVS is asymptotically stable if there are no external disturbances.

*Definition 2:* When disturbances are imposed on the head vehicle, a network is head-to-tail string stable if the disturbances are attenuated when reaching the tail vehicle.

Plant stability is a fundamental requirement for CVSs to avoid collisions. Assuming plant stability, head-to-tail string stability is used to determine disturbance attenuation that is required for congestion mitigation. We remark that head-to-tail string stability may not be satisfied for sufficiently large delays as will be shown in Sections IV and V.

*Remark:* Compared with the conventional definition of string stability [22], [23] that requires that disturbances are attenuated by each vehicle, head-to-tail string stability allows some vehicles in the network to amplify disturbances. This is particularly useful for CVSs that contain human-driven vehicles, as the dynamics of these vehicles cannot be designed. Head-to-tail string stability also allows one to compare the performance of different networks with same number of vehicles. In practice, disturbances may arise from any vehicles in a network, but the disturbances caused by the head vehicle pass through the whole vehicle network and hence have the greatest influence on the network performance. Therefore, head-to-tail string stability is particularly useful for characterizing disturbance attenuation in CVSs.

The stability of CVSs can be evaluated by using the head-to-tail transfer function, which represents the dynamic relationship between the head and the tail vehicles in the Laplace domain. Here, we develop an efficient method to calculate the head-to-tail transfer function, and also derive stability conditions by using this transfer function.

#### A. Calculation of Head-to-Tail Transfer Function

Consider an  $(n+1)$ -node network, where the head node and the tail node are indexed by 0 and  $n$ , respectively. Here,

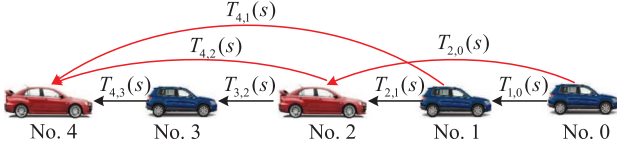


Fig. 3. Example of a connected vehicle network: link transfer functions are shown along the links.

each node represents a dynamic agent such as a vehicle. When omitting initial conditions, the Laplace transform of (10) yields

$$\tilde{Y}_i(s) = \sum_{j=p}^{i-1} T_{i,j}(s) \tilde{Y}_j(s) \quad (13)$$

where  $\tilde{Y}_i(s)$  denotes the Laplace transform of  $\tilde{y}_i(t)$  and

$$T_{i,j}(s) = \gamma_{i,j} e^{-s\xi_{i,j}} \mathbf{C} \left( s\mathbf{I}_2 - \mathbf{A}_0 - \sum_{j=p}^{i-1} \gamma_{i,j} e^{-s\xi_{i,j}} \mathbf{A}_{i,j} \right)^{-1} \times \mathbf{B}_{i,j} \mathbf{E}(s) \quad (14)$$

is called the *link transfer function* that acts as a dynamic gain along the network links; see the weighted graph Fig. 3. Here,  $\mathbf{I}_2$  denotes the 2-dimensional identity matrix and  $\mathbf{E}(s) = [s^{-1}, 1]^T$  links the state and the output of nodes such that  $\tilde{X}_j(s) = \mathbf{E}(s) \tilde{Y}_j(s)$ . Substituting (11) into (14) leads to

$$T_{i,j}(s) = \frac{\gamma_{i,j}(s\beta_{i,j} + \varphi_{i,j})e^{-s\xi_{i,j}}}{s^2 + \sum_{k=p}^{i-1} \gamma_{i,k}(s\kappa_{i,k} + \varphi_{i,k})e^{-s\xi_{i,k}}} \quad (15)$$

where  $\varphi_{i,j}$  and  $\kappa_{i,j}$  are given by (12).

The dynamic relationship between nodes  $i$  and  $m$  can be represented by the transfer function  $G_{i,m}(s)$  such that

$$\tilde{Y}_i(s) = G_{i,m}(s) \tilde{Y}_m(s). \quad (16)$$

Note that the transfer function  $G_{i,m}(s)$  includes the dynamics of all vehicles between vehicle  $m$  and vehicle  $i$ , and it can be obtained by using the relationship (13). To evaluate the performance of a network, we utilize the *head-to-tail transfer function* (HTTF)  $G_{n,0}(s)$ . Based on signal-propagation principles,  $G_{n,0}(s)$  can be calculated by summing up the products of link transfer functions along the paths connecting the nodes  $n$  and 0. However, finding these paths manually is difficult for complex networks. To address this problem systematically, one may use a graph theoretical approach [24]. Using the link transfer functions  $T_{i,j}(s)$  in (14), we define the dynamic coupling matrix  $\mathbf{T}(s) = [T_{i,j}(s)]$  where  $i, j = 0, \dots, n$ . Without loops, the longest path of an  $(n+1)$ -node network is of length  $n$ . Then, considering  $\mathbf{T}(s)$  as the adjacency matrix of a weighted graph, the transfer function matrix  $\mathbf{G}(s) = [G_{i,j}(s)]$ , where  $i, j = 0, \dots, n$ , can be calculated by

$$\mathbf{G}(s) = \sum_{k=1}^n (\mathbf{T}(s))^k. \quad (17)$$

However, when analyzing the network performance, we only need the HTTF  $G_{n,0}(s)$ . To directly calculate  $G_{n,0}(s)$ , we define the modified coupling matrix

$$\hat{\mathbf{T}}(s) = \mathbf{R}(\mathbf{T}(s) + \mathbf{I}_{n+1})\mathbf{R}^T \quad (18)$$

where  $\mathbf{R} = [\mathbf{0}_{n \times 1}, \mathbf{I}_n]$  and  $\mathbf{I}_n$  denotes the  $n$ -dimensional identity matrix while  $\mathbf{0}_{n \times 1}$  is an  $n$ -by-1 zero vector. Indeed,  $\hat{\mathbf{T}}(s)$  can be obtained by deleting the first row and last column of the matrix  $\mathbf{T}(s) + \mathbf{I}_{n+1}$ .

*Theorem 1:* Based on the matrix (18), the HTTF is given by

$$G_{n,0}(s) = \sum_{\sigma_i \in S_n} \prod_{i=1}^n \hat{T}_{i,\sigma_i}(s) = \frac{N(s)}{D(s)} \quad (19)$$

where the sum is computed over all permutations of the set  $S_n = \{1, 2, \dots, n\}$ .

Formula (19) is similar to the determinant of  $\hat{\mathbf{T}}(s)$  but does not include sign changes. The proof of Theorem 1 is given as follows. For an  $(n+1)$ -node network, the paths from node  $i$  to node  $n$  can be divided into two groups. One group contains node  $(i+1)$ , yielding the transfer function  $G_{n,i+1}(s)T_{i+1,i}(s)$ . The other group does not contain node  $(i+1)$  but includes the long links connecting nodes  $i$  and  $n$ , leading to the transfer function  $\bar{G}_{n,i}(s)$ . That is, we have  $G_{n,i}(s) = G_{n,i+1}(s)T_{i+1,i}(s) + \bar{G}_{n,i}(s)$ . Applying this formula recursively from  $i = 0$  to  $i = n-2$  leads to (19), which completes the proof.

To demonstrate the applications of (17) and (19), we consider the network in Fig. 3 as an example and calculate the HTTF in Appendix A.

## B. Plant Stability and Head-to-Tail String Stability

Here, we present delay-dependent criteria for plant stability and head-to-tail string stability by using the HTTF (19). The delays  $\xi_{i,j}$  lead to infinitely many characteristic roots  $s_i$  ( $i = 1, 2, \dots$ ) that satisfy the characteristic equation  $D(s) = 0$ . Since the negative real parts of characteristic roots indicate the decay of initial perturbation, a system is plant stable if and only if

$$\text{Re}(s_i) < 0, \quad i = 1, 2, \dots \quad (20)$$

Sufficient stability conditions may be derived by using approximations and inequalities, but such results may be quite conservative. To obtain exact (necessary & sufficient) stability conditions, we utilize the D-subdivision method [25] and seek for plant stability boundaries, which correspond to purely imaginary characteristic roots  $\pm j\Omega$  ( $j^2 = -1, \Omega \geq 0$ ) that satisfy  $D(\pm j\Omega) = 0$ . This is equivalent to

$$\text{Re}(D(j\Omega)) = 0, \quad \text{Im}(D(j\Omega)) = 0. \quad (21)$$

Solving this for  $\alpha_n(\Omega)$  and  $\beta_n(\Omega)$  with  $\Omega > 0$  leads to plant stability boundaries in the  $(\beta_n, \alpha_n)$ -plane. For  $\Omega = 0$ , since  $D(0)$  becomes a real number, the condition (21) can be reduced to

$$D(0) = 0 \quad (22)$$

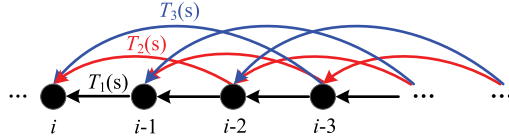


Fig. 4. A network with a repetitive structure, where each node responds to the nearest three nodes ahead.

which yields additional plant stability boundaries in the  $(\beta_n, \alpha_n)$ -plane.

Based on the HTTF (19), a disturbance with frequency  $\omega$  from the head vehicle will be amplified by the ratio  $|G_{n,0}(j\omega)|$  when reaching the tail vehicle. Thus, a vehicle network is head-to-tail string stable if and only if

$$|G_{n,0}(j\omega)| < 1, \quad \forall \omega > 0. \quad (23)$$

At the boundary, we have  $\max_{\omega} |G_{n,0}(j\omega)| = 1$ , which is equivalent to

$$|G_{n,0}(j\omega_{cr})| = 1, \quad |G_{n,0}(j\omega_{cr})'| = 0, \quad |G_{n,0}(j\omega_{cr})''| < 0 \quad (24)$$

where the prime denotes the partial derivative with respect to  $\omega$ , while  $\omega_{cr}$  is the critical frequency where the maximum occurs. Solving (24) for  $\alpha_n(\omega_{cr})$  and  $\beta_n(\omega_{cr})$  gives the head-to-tail string stability boundaries in the  $(\beta_n, \alpha_n)$ -plane. For vehicle networks (10)–(12),  $|G_{n,0}(0)| = 1$  and  $|G_{n,0}(0)'| = 0$  always hold. Thus, head-to-tail string stability boundaries for  $\omega_{cr} = 0$  result from

$$|G_{n,0}(0)|'' = 0. \quad (25)$$

Stability diagrams can be constructed by combining boundaries ((21), (22), (24), (25)), as will be shown in following sections.

The head-to-tail string stability condition (23) requires the calculation of HTTF which is challenging for large networks. This motivates us to seek for stability conditions that are scalable when network size increases. Indeed, such conditions may not exist for general networks. Here, we focus on a class of networks with repetitive connectivity structures where each node utilizes information received from the nearest  $\ell$  nodes ahead; see Fig. 4 for  $\ell = 3$ . Such networks can be realized by using chains of identical CCC vehicles. In this case, the link transfer function of the same length are identical, i.e.,  $T_{i,j}(s) = T_{i-j}(s)$ . Substituting this into (13) yields

$$\tilde{Y}_i(s) = \sum_{k=1}^{\ell} T_k(s) \tilde{Y}_{i-k}(s), \quad i \geq \ell \quad (26)$$

where  $T_k(s)$  is the link transfer function for links of length  $k$ . Note that (16) implies that  $\tilde{Y}_{i-k}(s) = G_{i-k,0}(s) \tilde{Y}_0(s)$ . Combining this with (26) yields the recursive formula

$$G_{i,0}(s) = \sum_{k=1}^{\ell} T_k(s) G_{i-k,0}(s), \quad i \geq \ell \quad (27)$$

which can be rewritten into the matrix form

$$\hat{G}_i(s) = \hat{\mathbf{P}}(s) \hat{G}_{i-1}(s) \quad (28)$$

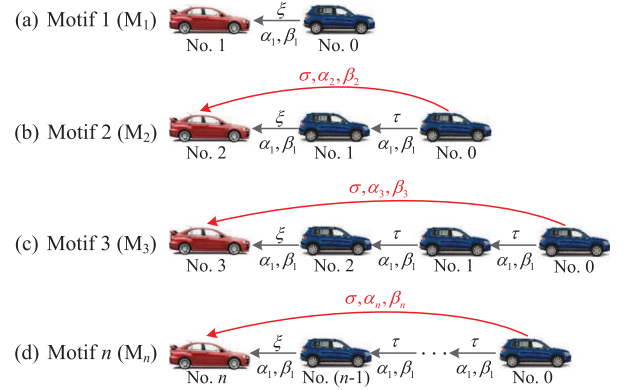


Fig. 5. Network motifs 1, 2, 3, and  $n$ . Symbols  $\tau$ ,  $\sigma$ ,  $\xi$  denote information delays while  $\alpha_k, \beta_k$  are control gains along the link of length  $k$  for  $k = 1, 2, \dots$

where

$$\hat{G}_i(s) = [G_{i,0}(s) \quad G_{i-1,0}(s) \quad \dots \quad G_{i-\ell}(s)]^T$$

$$\hat{\mathbf{P}}(s) = \begin{bmatrix} T_1(s) & T_2(s) & \dots & T_{\ell-1}(s) & T_{\ell}(s) \\ 1 & 0 & \dots & 0 & 0 \\ 0 & 1 & \dots & 0 & 0 \\ \vdots & \vdots & \ddots & \vdots & \vdots \\ 0 & 0 & \dots & 1 & 0 \end{bmatrix}. \quad (29)$$

Then for networks with repetitive structures (26)–(29), we provide a condition that guarantees disturbance attenuation as a network scales up.

**Theorem 2:** For the networks with repetitive structures (26), as the network size increases to infinity, the disturbance on the tail is attenuated to zero if and only if

$$\sup_{\omega > 0} \left| \lambda_k \left( \hat{\mathbf{P}}(j\omega) \right) \right| < 1, \quad k = 1, \dots, \ell \quad (30)$$

where  $\lambda_k(\hat{\mathbf{P}}(j\omega))$  denotes the  $k$ -th eigenvalue of  $\hat{\mathbf{P}}(j\omega)$  in (29).

Note that (28) can be seen as a discrete system in terms of the vehicle index  $i$ . Based on the linear discrete system theory [26], we have that  $\lim_{i \rightarrow \infty} \|\hat{G}_i(j\omega)\| = 0$  for  $\forall \omega > 0$  if and only if the condition (30) holds. This completes the proof for Theorem 2. Note that condition (30) only utilizes link transfer functions without calculating the HTTF. This reduces the complexity of analysis and design for large networks.

#### IV. NETWORK MOTIFS AND THEIR STABILITY

In this section, we define network motifs in CVSs and investigate their stability. In general, network motifs are recurrent subnetworks in complex networks [19]. In CVSs, we define motif  $n$  (denoted by  $M_n$ ) as follows.

**Definition 3:** Motif  $n$  ( $M_n$ ) is a network where a CCC vehicle exploits information received from the vehicle immediately ahead and the vehicle that is  $n$ -vehicles away, while all the other vehicles only respond to the motion of the vehicle immediately ahead.

Fig. 5 shows motifs for different values of  $n$ . The advantage of the motif-based approach is that, by analyzing the dynamics of motifs and characterizing the effects of motif combinations, one may modularly design robust CVSs which remain scalable when the network size increases.



Characterizing the system dynamics with a large number of independent parameters is typically not feasible. To make the analysis tractable while keeping the essential heterogeneity, we make the following assumptions. First, we consider three kinds of delays: human reaction time, sensing delay, and communication delay. We assume that the same kind of delays have the same value. Specifically, we use  $\tau \approx 0.5\text{--}1.5$  [s] for human reaction time and use  $\sigma \approx 0.1\text{--}0.4$  [s] for communication delay. The symbol  $\xi$  may represent human reaction time ( $\xi = \tau$ ) if CCC is used to assist a human driver, communication delay ( $\xi = \sigma$ ) if the CCC vehicle is automatically controlled based on communication, or sensing delay  $\xi \approx 0.1\text{--}0.2$  [s] if the CCC vehicle is equipped with range sensors. Communication delays arise from intermittency and packet drops [27], and they may vary stochastically in time [28]. In this paper, we approximate communication delays by using their mean values. Moreover, we assume that the control gains for links of length  $k$  are the same and denoted by  $\alpha_k, \beta_k$ ; see Fig. 5. Finally, we assume that human drivers can be modeled by using the framework (2) with  $\gamma_{i,i-1} = 1$  and  $\gamma_{i,j} = 0$  for  $j \neq i-1$ . This human driver model has been validated by using traffic data in [29].

Hence, applying (2) to each vehicle in  $M_n$  leads to

$$\begin{aligned}\dot{s}_j(t) &= v_j(t) \\ \dot{v}_j(t) &= \alpha_1 (V(h_{j,j-1}(t-\tau)) - v_j(t-\tau)) \\ &\quad + \beta_1 (v_{j-1}(t-\tau) - v_j(t-\tau)) \\ \dot{s}_n(t) &= v_n(t) \\ \dot{v}_n(t) &= \alpha_1 (V(h_{n,n-1}(t-\xi)) - v_n(t-\xi)) \\ &\quad + \beta_1 (v_{n-1}(t-\xi) - v_n(t-\xi)) \\ &\quad + \alpha_n (V(h_{n,0}(t-\sigma)) - v_n(t-\sigma)) \\ &\quad + \beta_n (v_0(t-\sigma) - v_n(t-\sigma))\end{aligned}\quad (31)$$

for  $j = 1, \dots, n-1$ . The network  $M_1$  contains only one following vehicle so that its dynamics is governed by the first two equations in (31) but with delay  $\xi$ . Considering the worst-case scenario for robustness, we assume that all vehicles (including the CCC vehicle) are driven by human drivers. Thus, the stability diagrams are generated for  $\xi = \tau$ , although formulae are derived for general delay  $\xi$ .

Linearizing (31) about the equilibrium ((7), (8)) yields

$$\begin{aligned}\dot{\tilde{x}}_j(t) &= \mathbf{A}_0 \tilde{x}_j(t) + \mathcal{D}_\tau (\mathbf{A}_1 \tilde{x}_j + \mathbf{B}_1 \tilde{x}_{j-1}(t)) \\ \tilde{y}_j(t) &= \mathbf{C} \tilde{x}_j(t) \\ \dot{\tilde{x}}_n(t) &= \mathbf{A}_0 \tilde{x}_n(t) + \mathcal{D}_\xi (\mathbf{A}_1 \tilde{x}_n(t) + \mathbf{B}_1 \tilde{x}_{n-1}(t)) \\ &\quad + \mathcal{D}_\sigma (\mathbf{A}_n \tilde{x}_n(t) + \mathbf{B}_n \tilde{x}_0(t)) \\ \tilde{y}_n(t) &= \mathbf{C} \tilde{x}_n(t)\end{aligned}\quad (32)$$

for  $j = 1, \dots, n-1$ , where the matrices are given by

$$\mathbf{A}_m = \begin{bmatrix} 0 & 0 \\ -\varphi_m & -\kappa_m \end{bmatrix}, \quad \mathbf{B}_m = \begin{bmatrix} 0 & 0 \\ \varphi_m & \beta_m \end{bmatrix}\quad (33)$$

and

$$\varphi_m = \frac{\alpha_m V'(h^*)}{m}, \quad \kappa_m = \alpha_m + \beta_m\quad (34)$$

for  $m = 1, \dots, n$ ; cf. (10)–(12).

Corresponding to the connectivity structure of  $M_n$ , formula (15) leads to the link transfer functions

$$\begin{aligned}T_{j,j-1}(s) &= \frac{\beta_1 s + \varphi_1}{s^2 e^{s\tau} + \kappa_1 s + \varphi_1} := T_h(s) \\ T_{n,n-1}(s) &= \frac{(\beta_1 s + \varphi_1) e^{s(\sigma-\xi)}}{s^2 e^{s\sigma} + (\kappa_1 s + \varphi_1) e^{s(\sigma-\xi)} + \kappa_n s + \varphi_n} \\ T_{n,0}(s) &= \frac{\beta_n s + \varphi_n}{s^2 e^{s\sigma} + (\kappa_1 s + \varphi_1) e^{s(\sigma-\xi)} + \kappa_n s + \varphi_n}\end{aligned}\quad (35)$$

for  $j = 1, \dots, n-1$ , where  $T_h(s)$  denotes the link transfer function for human-driven vehicles. Applying (19) yields the head-to-tail transfer function

$$G_{n,0}(s) = (T_h(s))^{n-1} T_{n,n-1}(s) + T_{n,0}(s).\quad (36)$$

First, we investigate the plant stability of  $M_n$ . Substituting (35) into (36) leads to the characteristic equation

$$\begin{aligned}D(s) &= (s^2 e^{s\tau} + \kappa_1 s + \varphi_1)^{n-1} \\ &\quad \times (s^2 e^{s\sigma} + (\kappa_1 s + \varphi_1) e^{s(\sigma-\xi)} + \kappa_n s + \varphi_n) = 0\end{aligned}\quad (37)$$

where the first term is indeed the characteristic polynomial of  $M_1$ . When  $\Omega > 0$ , substituting (37) into (21), the first term yields

$$\begin{aligned}\alpha_1 &= \frac{\Omega^2 \cos(\Omega\tau)}{V'(h^*)} \\ \beta_1 &= \Omega \sin(\Omega\tau) - \alpha_1\end{aligned}\quad (38)$$

while the second term results in

$$\begin{aligned}\alpha_n &= \frac{n}{V'(h^*)} [\Omega^2 \cos(\Omega\sigma) - \varphi_1 \cos(\Omega(\sigma-\xi)) \\ &\quad + \kappa_1 \Omega \sin(\Omega(\sigma-\xi))] \\ \beta_n &= \Omega \sin(\Omega\sigma) - \frac{\varphi_1}{\Omega} \sin(\Omega(\sigma-\xi)) \\ &\quad - \kappa_1 \cos(\Omega(\sigma-\xi)) - \alpha_n\end{aligned}\quad (39)$$

for  $n > 1$ . When  $\Omega = 0$ , substituting (37) into (22) while considering (34) leads to the plant stability boundary

$$\alpha_n = -n\alpha_1.\quad (40)$$

Using ((35), (36)) in (24) yields the head-to-tail string stability boundary

$$\begin{aligned}\alpha_n &= \frac{-2\omega_{cr}^2 Q_1 + P_1 + P_2 Q_2 \pm \sqrt{\Delta}}{2\omega_{cr}^2 (1 + 2Q_2)} \\ \beta_n &= Q_1 + Q_2 \alpha_n\end{aligned}\quad (41)$$

for  $\omega_{cr} > 0$  and  $n > 1$ , where  $P_1, P_2, Q_1, Q_2, \Delta$  are given in Appendix B. For  $\omega_{cr} = 0$ , we use ((35), (36)) in (25) and obtain the head-to-tail string stability boundaries

$$\alpha_n = -n\alpha_1\quad (42)$$

and

$$\alpha_n = -2\beta_n - \alpha_1 + 2(V'(h^*) - \beta_1).\quad (43)$$

Plotting the stability boundaries (38)–(43) in the plane of control gains  $\alpha_n$  and  $\beta_n$  results in stability diagrams, as will be shown in the rest of this paper.

#### A. Stability Diagrams for Motif 1

The head-to-tail transfer function of motif  $M_1$  is  $G_{1,0}(s) = T_h(s)$  with delay  $\xi$ ; cf. ((35), (36)). The plant stability boundaries of  $M_1$  are given by (38) and (40). For  $\omega_{cr} > 0$ , head-to-tail string stability boundaries (41) can be simplified to

$$\alpha_1 = \frac{1}{R_3} \left( R_2 \pm \sqrt{R_2^2 + R_3 R_1} \right)$$

$$\beta_1 = \frac{\alpha_1 ((V'(h^*)\xi - 1) \sin(\omega_{cr}\xi) - \omega_{cr}\xi \cos(\omega_{cr}\xi)) + \omega_{cr}}{\sin(\omega_{cr}\xi) + \omega_{cr}\xi \cos(\omega_{cr}\xi)} \quad (44)$$

where

$$R_1 = \omega_{cr}^2 (\sin(\omega_{cr}\xi) - \omega_{cr}\xi \cos(\omega_{cr}\xi))$$

$$R_2 = V'(h^*) (\omega_{cr}\xi + \sin(\omega_{cr}\xi) \cos(\omega_{cr}\xi)) - \omega_{cr}$$

$$R_3 = (2V'(h^*)\xi - 1) \sin(\omega_{cr}\xi) - \omega_{cr}\xi \cos(\omega_{cr}\xi). \quad (45)$$

For  $\omega_{cr} = 0$ , using  $\alpha_n = \beta_n = 0$  in (42) and (43) yields

$$\alpha_1 = 0 \quad (46)$$

$$\alpha_1 = 2(V'(h^*) - \beta_1), \quad (47)$$

respectively.

The stability diagram of motif  $M_1$  is shown in Fig. 6(a) for the delay  $\xi = 0.2$  [s], where the plant stable domain and the head-to-tail string stable domain are shaded by light gray and dark gray, respectively. The red curves denote the plant stability boundaries ((38), (40)) while the blue curves represent the head-to-tail string stability boundaries (44)–(47). These notations are used in the stability diagrams in the rest of this paper. Fig. 6(b) shows the frequencies  $\Omega$  and  $\omega_{cr}$ , at which  $M_1$  loses plant stability and head-to-tail string stability, respectively.

In Fig. 6(a), points A–C are marked to show how plant stability changes when control gains are varied. Fig. 6(d)–(f) show the corresponding leading characteristic roots, which are obtained by using the numerical continuation package DDE-BIFTOOL [30]. When crossing the plant stability boundary, a pair of complex conjugate characteristic roots moves to the right half complex plane. That is,  $M_1$  loses plant stability through a Hopf bifurcation. Points C–G are marked to show how string stability changes with control gains. The corresponding Bode plots are depicted in Fig. 6(c). Case E shows a string stable scenario where  $|G_{1,0}(j\omega)| < 1$  for  $\forall \omega > 0$ . When crossing the boundary for  $\omega_{cr} > 0$  (case D), the system becomes string unstable for mid-range frequencies (case C). On the other hand, case F shows marginal string stability at  $\omega_{cr} = 0$ , implying string instability for low frequencies in case G.

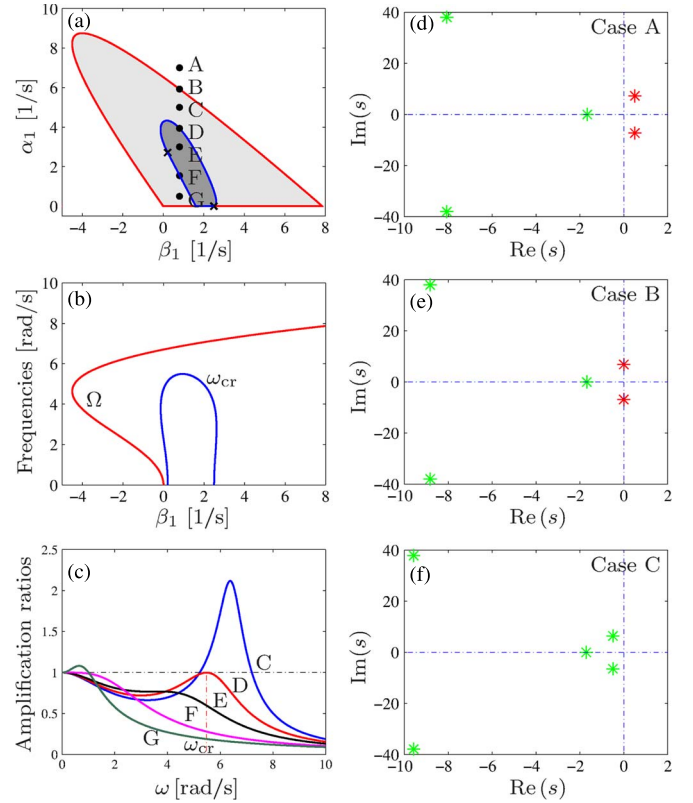


Fig. 6. (a): Stability diagram of motif  $M_1$  for delay  $\xi = 0.2$  [s], showing the plant stable domain (light gray) and the head-to-tail string stable domain (dark gray). The red and blue curves represent the plant stability boundaries ((38), (40)) and the head-to-tail string stability boundaries (44)–(47), respectively. (b): Frequencies  $\Omega$  for plant stability (red curve) and  $\omega_{cr}$  for head-to-tail string stability (blue curve). (c): Bode plots corresponding to cases C–G. (d)–(f): Leading characteristic roots for cases A–C.

The stability diagrams of motif  $M_1$  are compared in Fig. 7 for different values of delay  $\xi$ , where the same notation is used as in Fig. 6(a). When the delay  $\xi$  increases, the stable domains shrink and the head-to-tail string stable domain disappears for a sufficiently large delay. To calculate the critical delay, we investigate how the “anchor points” (marked by crosses) move as  $\xi$  is varied. Substituting  $\omega_{cr} = 0$  into (44) and applying L’Hospital’s rule gives the locations of the two crosses:

$$(\alpha_1^-, \beta_1^-) = \left( \frac{2V'(h^*)\xi - 1}{\xi(V'(h^*)\xi - 1)}, \frac{2(V'(h^*)\xi)^2 - 4V'(h^*)\xi + 1}{2\xi(V'(h^*)\xi - 1)} \right)$$

$$(\alpha_1^+, \beta_1^+) = \left( 0, \frac{1}{2\xi} \right). \quad (48)$$

The head-to-tail string stable domain disappears when these points meet at  $(V'(h^*), 0)$ , i.e.,  $\beta_1^- = \beta_1^+ = V'(h^*)$  and  $\alpha_1^- = \alpha_1^+ = 0$ , yielding the critical delay

$$\xi_{cr} = \frac{1}{2V'(h^*)} = \frac{T_{gap}}{2}. \quad (49)$$

If  $\xi > \xi_{cr}$ , the head-to-tail string stability of  $M_1$  cannot be achieved for any gain combinations. For the range policy ((4), (6)) at  $h^* = 20$  [m], we get  $\xi_{cr} \approx 0.325$  [s].

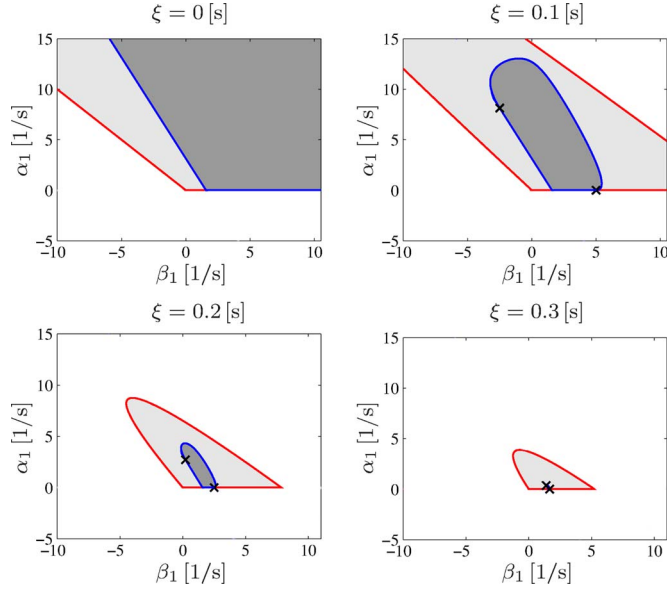


Fig. 7. Stability diagrams of motif  $M_1$  for different values of delay  $\xi$  as indicated. The same notations are used as in Fig. 6(a).

In the remaining part of this paper, we assume the human reaction time  $\tau = 0.5$  [s], which is larger than the critical delay. This implies that human drivers typically cannot maintain string stability in the mid-headway range. We also assume the control gains  $\alpha_1 = 0.6$  [1/s] and  $\beta_1 = 0.7$  [1/s], that is, the human-driven vehicles are plant stable but string unstable. These parameters will be used for other motifs and motif combinations.

### B. Stability Diagrams for Motif $n$ ( $n > 1$ )

For motif  $M_n$  ( $n > 1$ ), we consider a conservative case where all vehicles (including the CCC vehicle) are driven by human drivers. Using (39)–(43), the stability diagram for  $M_2$  is depicted in Fig. 8(a) for the communication delay  $\sigma = 0.2$  [s]. The corresponding frequencies  $\Omega$  and  $\omega_{cr}$  are shown in Fig. 8(e). Points H and I are marked in Fig. 8(a) to illustrate how the head-to-tail string stability changes when the control gains are varied. In case H ( $\alpha_2 = \beta_2 = 0$ ), the V2V communication is not utilized, which leads to the amplification of low-frequency disturbances; see Fig. 8(b). In case I, the CCC vehicle 2 exploits the communication and utilizes the motion data of vehicle 0. The Bode plot in Fig. 8(c) shows that the CCC vehicle 2 can attenuate disturbances at all frequencies even though vehicle 1 amplifies them.

We also demonstrate this phenomenon by simulating the nonlinear model (31), as shown in Fig. 8(f) and (g). Here, the velocity of vehicle 0 is assumed to be  $v_0(t) = v^* + v_{amp} \sin(\omega t)$ , where the sinusoidal term denotes the disturbance. Specifically, we use  $v^* = 15$  [m/s],  $v_{amp} = 1$  [m/s],  $\omega = 1.45$  [rad/s], and assume the initial headways  $h_1(t) \equiv 19$  [m],  $h_2(t) \equiv 21$  [m] and initial velocities  $v_1(t) \equiv 12$  [m/s],  $v_2(t) \equiv 16$  [m/s] along the time interval  $t \in [-\tau, 0]$ . Indeed, vehicle 1 amplifies the disturbance in both cases, while vehicle 2 further amplifies it in case H but attenuates it in case I.

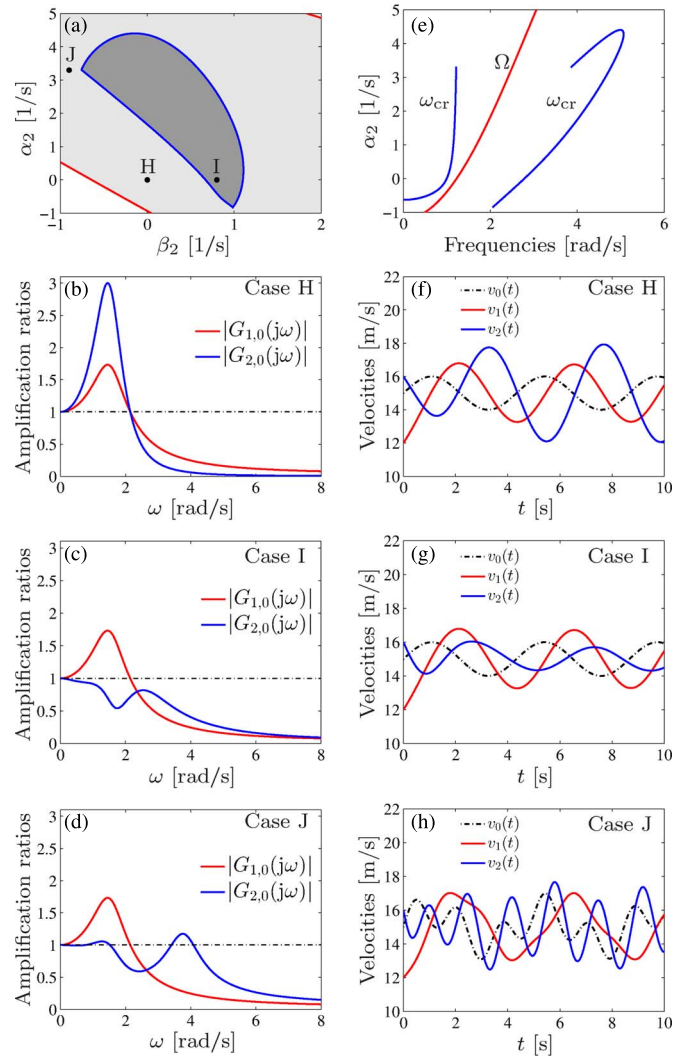


Fig. 8. (a): Stability diagram of motif  $M_2$  when  $\alpha_1 = 0.6$  [1/s],  $\beta_1 = 0.7$  [1/s],  $\tau = 0.5$  [s], and  $\sigma = 0.2$  [s]. The same notation is used as in Fig. 6(a). (b)–(d): Bode plots for cases H–J. (e): Frequencies corresponding to the stability boundaries in panel (a). (f)–(h): Simulation results for cases H–J.

For motifs  $M_n$  ( $n > 1$ ), head-to-tail string instability may occur for multiple frequency ranges due to the intersection of head-to-tail string stability boundaries for different values of  $\omega_{cr} > 0$ ; cf. blue curves in Fig. 8(e). Point J is marked in the vicinity of the intersection in Fig. 8(a) and the corresponding Bode plot is displayed in Fig. 8(d), which shows that  $|G_{2,0}(j\omega)| \geq 1$  in two distinct frequency ranges. To demonstrate this performance, simulations are carried out using the nonlinear model (31) and the results are shown in Fig. 8(h). The velocity of vehicle 0 is prescribed as  $v_0(t) = v^* + v_{amp,1} \sin(\omega_1 t) + v_{amp,2} \sin(\omega_2 t)$  with  $v^* = 15$  [m/s],  $v_{amp,1} = 1$  [m/s],  $v_{amp,2} = 1$  [m/s],  $\omega_1 = 1.45$  [rad/s], and  $\omega_2 = 3.75$  [rad/s], where  $\omega_1$  and  $\omega_2$  are selected from the first and the second string unstable frequency ranges, respectively. The simulation result in Fig. 8(h) indicates that vehicle 2 amplifies the disturbances for both frequencies, while vehicle 1 only amplifies the low-frequency disturbance. This implies that CCC vehicles may deteriorate the performance of traffic flow if the control gains are not appropriately designed.



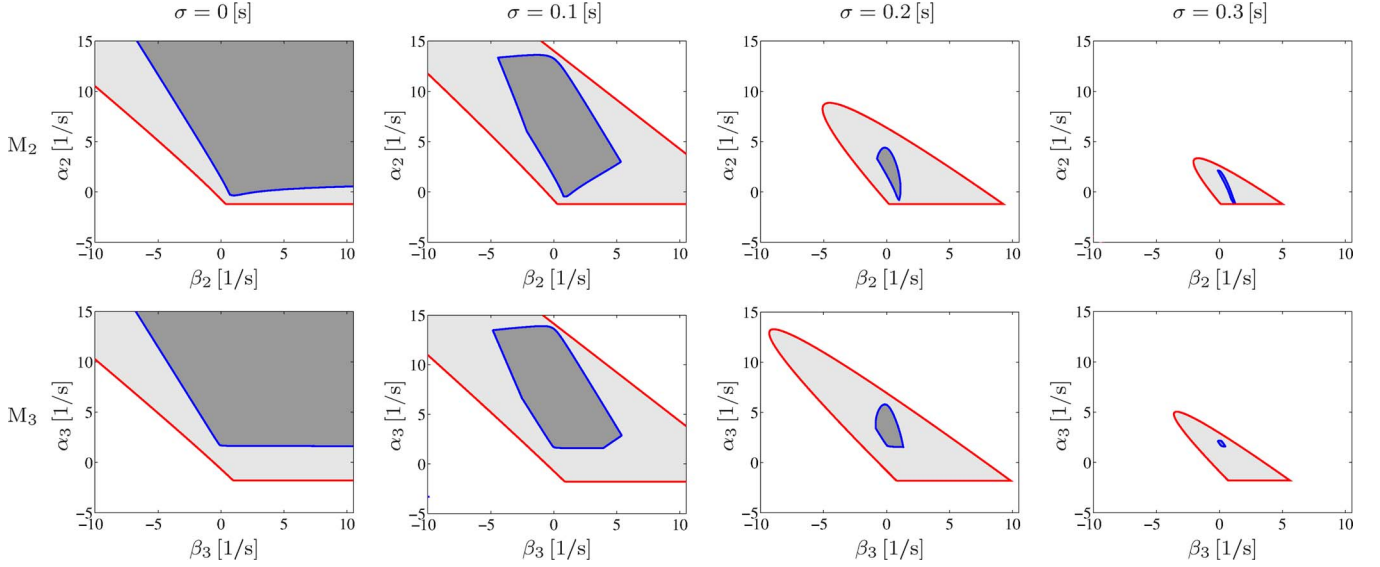


Fig. 9. Stability diagrams for motifs  $M_2$  (top row) and  $M_3$  (bottom row) for different values of the communication delay  $\sigma$  when  $\alpha_1 = 0.6$  [1/s],  $\beta = 0.7$  [1/s], and  $\tau = 0.5$  [s]. The same notation is used as in Fig. 6(a).

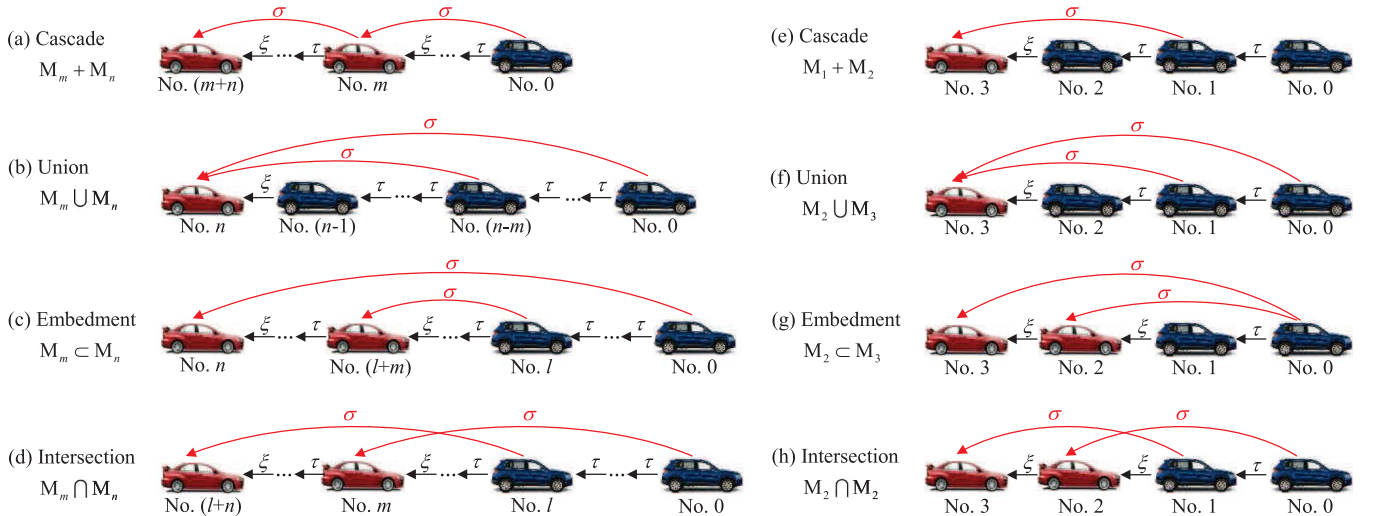


Fig. 10. Motif combinations (left column) and corresponding examples for (3+1)-vehicle networks (right column).

For different values of communication delay  $\sigma$ , we display stability diagrams for  $M_2$  and  $M_3$  in Fig. 9. Note that control gains  $\alpha_2$ ,  $\beta_2$  are used for  $M_2$  while  $\alpha_3$ ,  $\beta_3$  are used for  $M_3$ . As  $\sigma$  increases, head-to-tail string stable domains decrease and disappear for  $\sigma_{cr} \gtrsim 0.3$  [s], which is larger than the typical communication delay  $\sigma = 0.1$ – $0.2$  [s]. The stability diagrams for  $M_3$  imply that the CCC vehicle may ensure the head-to-tail string stability for a network which contains more than one vehicles that amplify disturbances.

## V. MOTIF COMBINATIONS

In this section, we investigate the effects of motif combinations on the dynamics of complex vehicle networks. In particular, we construct vehicle networks by using the motif combinations *cascade*, *union*, *embedment*, and *intersection*, which are denoted by “+,” “ $\cup$ ,” “ $\subset$ ” and “ $\cap$ ,” respectively. Fig. 10(a)–(d) depict these combinations for general motifs  $M_m$

and  $M_n$  ( $n > m > 1$ ) while specific examples are presented in Fig. 10(e)–(h) for 4 vehicles.

Cascades and intersections are defined literally. A union of motifs is obtained when the CCC vehicle utilizes information from multiple distant vehicles ahead. Particularly, for  $M_1 \cup M_2 \cup \dots \cup M_n$ , the CCC vehicle maximizes the use of V2V communication; see Fig. 1 and Fig. 10(f). A combination is called embedment if a motif is entirely enclosed by another motif without intersection of links. In this case, each CCC vehicle only receives information from one distant vehicle. We remark that CACC can be seen as a particular embedment network where all vehicles monitor a designated leader; see Fig. 10(g).

### A. Cascade of Motifs

Cascade networks can be realized by placing motifs one after another. Particularly, the cascade of  $M_1$ 's represents the conventional car-following scenario where each vehicle only

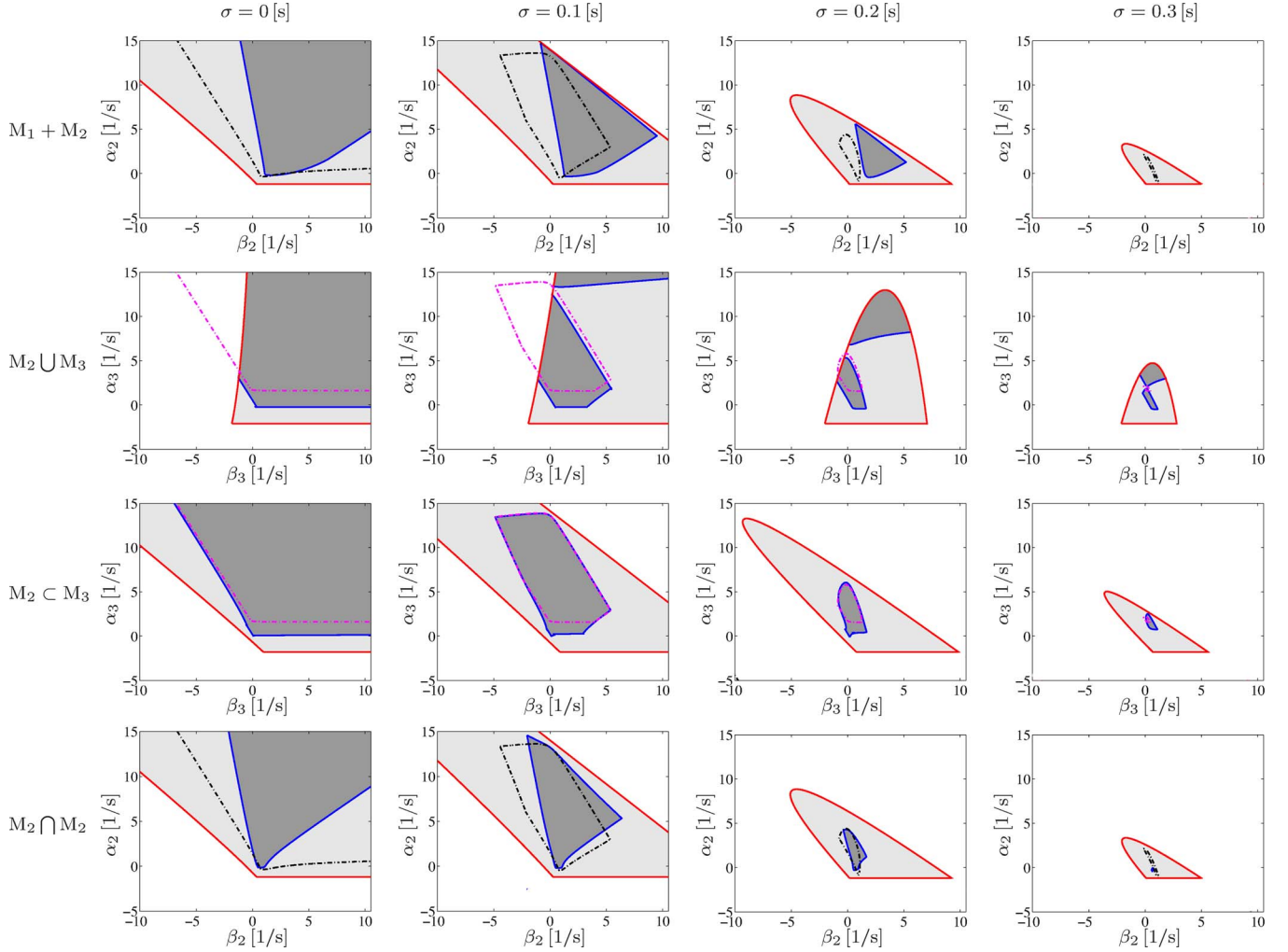


Fig. 11. Stability diagrams for cascade  $M_1 + M_2$  (first row), union  $M_2 \cup M_3$  (second row), embedment  $M_2 \subset M_3$  (third row) and intersection  $M_2 \cap M_2$  (fourth row) for  $\alpha_1 = 0.6$  [1/s],  $\beta_1 = 0.7$  [1/s],  $\xi = \tau = 0.5$  [s], and different values of the communication delay  $\sigma$  as indicated. For  $M_2 \cup M_3$  and  $M_2 \subset M_3$ ,  $\alpha_2 = 0$  [1/s] and  $\beta_2 = 0.8$  [1/s] are also used. The same notation is used as in Fig. 6(a). For comparison, the stability boundaries of  $M_2$  and  $M_3$  are given by the dashed-dotted black and magenta curves, respectively.

responds to the motion of the vehicle immediately ahead. Indeed, the stability of a cascade network can be ensured by the stability of each included motif, as stated in the following theorem.

**Theorem 3:** A cascade network is

- 1) plant stable if and only if each included motif is plant stable;
- 2) head-to-tail string stable if each included motif is head-to-tail string stable.

Since the HTTF of a cascade network results from the product of the transfer functions of all included motifs, the following two facts hold. 1) The characteristic roots of the cascade network are indeed the characteristic roots of all included motifs; 2) The head-to-tail amplification ratio of the cascade network is the product of the amplification ratios of all included motifs. Then, the proof of Theorem 3 can be completed by using the aforementioned two facts in the conditions (20) and (23), respectively.

Note that 2) in Theorem 3 is only a sufficient condition. It implies that a cascade network can be still head-to-tail

string stable even when some motifs in it amplify disturbances. To demonstrate this, we investigate the network  $M_1 + M_2$  (Fig. 10(e)). In this case, according to (19), the HTTF is

$$G_{3,0}(s) = T_h(s) (T_{3,1}(s) + T_{3,2}(s)T_h(s)) \quad (50)$$

where the link transfer functions  $T_h(s)$ ,  $T_{3,1}(s) = T_{2,0}(s)$ ,  $T_{3,2}(s) = T_{2,1}(s)$  are given in (35). The human-driven vehicles 1 and 2 amplify disturbances due to large human reaction time; see Section IV-A.

Then, using (50) in (21)–(25), one can construct the stability diagrams in the  $(\beta_2, \alpha_2)$ -plane, as displayed in the top row of Fig. 11, which imply that the CCC vehicle 3 can attenuate disturbances of vehicle 0 when  $\sigma \lesssim 0.2$  [s]. Comparing the stable domains of  $M_1 + M_2$  with those of  $M_2$  (enclosed by black dashed-dotted curve), one may notice that for  $M_1 + M_2$  the head-to-tail string stable domain disappears for  $\sigma = 0.3$  [s], while  $M_2$  can still be stabilized for this delay value. This implies that including string unstable motifs in the cascade may decrease the robustness of the network against communication delays.

### B. Union of Motifs

A union network is formed when a CCC vehicle utilizes information from multiple distant vehicles ahead. The network  $M_1 \cup M_2 \cup \dots \cup M_n$  can be observed in Fig. 1 setting  $p = 0$  and  $i = n$ . Based on (19), we obtain the HTTF

$$G_{n,0}(s) = \sum_{j=0}^{n-1} T_{n,j}(s) (T_h(s))^j \quad (51)$$

where the link transfer functions  $T_{n,j}(s)$  and  $T_h(s)$  are given by (15) and (35), respectively.

Here, we investigate  $M_2 \cup M_3$  (Fig. 10(f)). For  $M_2$ , we set  $\alpha_2 = 0$  [1/s] and  $\beta_2 = 0.8$  [1/s] (see case I in Fig. 8(a)). This ensures that, if vehicles 0 and 3 disconnect,  $M_2$  (comprised of vehicles 1,2,3) is still head-to-tail string stable. Substituting (51) into (21)–(25) with  $n = 4$ , one may generate stability diagrams in the  $(\beta_3, \alpha_3)$ -plane, as shown in the second row of Fig. 11. Comparing these stable domains with those of  $M_3$  (enclosed by magenta dashed-dotted curve), one may observe that using more communication links can improve the robustness against communication delays.

### C. Embedment of Motifs

For the embedment  $M_m \subset M_n$  ( $1 < m < n$ ) shown in Fig. 10(c), we utilize (19) and get the HTTF

$$G_{n,0}(s) = T_{n,0}(s) + T_{n,n-1}(s) (T_h(s))^{n-m-1} \times \left( T_{l+m,l+m-1}(s) (T_h(s))^{m-1} + T_{l+m,l}(s) \right) \quad (52)$$

where link transfer functions are given by (35) such that  $T_{l+m,l+m-1}(s)$  and  $T_{l+m,l}(s)$  are equal to  $T_{m,m-1}(s)$  and  $T_{m,0}(s)$ , respectively.

Substituting (52) into (21)–(25) with  $m = 2$  and  $n = 3$ , one can construct the stability diagrams for  $M_2 \subset M_3$ , as shown in the third row of Fig. 11. The head-to-tail string stable domains of  $M_2 \subset M_3$  are larger than those of  $M_3$  (enclosed by magenta dashed-dotted curves). These imply that embedding CCC vehicles in the network may enlarge the head-to-tail string stable domain. Comparing the stability diagrams for  $M_2 \cup M_3$  and  $M_2 \subset M_3$  (the second and the third rows of Fig. 11), one may observe that utilizing motion data received from multiple vehicles improves the robustness against communication delays. Moreover, using union instead of embedment decreases the required number of CCC vehicles to stabilize the network.

### D. Intersection of Motifs

Intersection networks can be comprised of any motifs. Here, we focus on  $M_2$  intersections where each CCC vehicle monitors the vehicle that is two vehicles ahead, which results in a network with a repetitive structure; cf. Fig. 4. We begin with  $M_2 \cap M_2$  (Fig. 10(h)), for which (19) gives the HTTF

$$G_{3,0}(s) = T_{3,1}(s)T_h(s) + T_{3,2}(s)(T_{2,1}(s)T_h(s) + T_{2,0}(s)) \quad (53)$$

where the link transfer functions  $T_h(s)$ ,  $T_{3,2}(s) = T_{2,1}(s)$ , and  $T_{3,1}(s) = T_{2,0}(s)$  are given by (35).

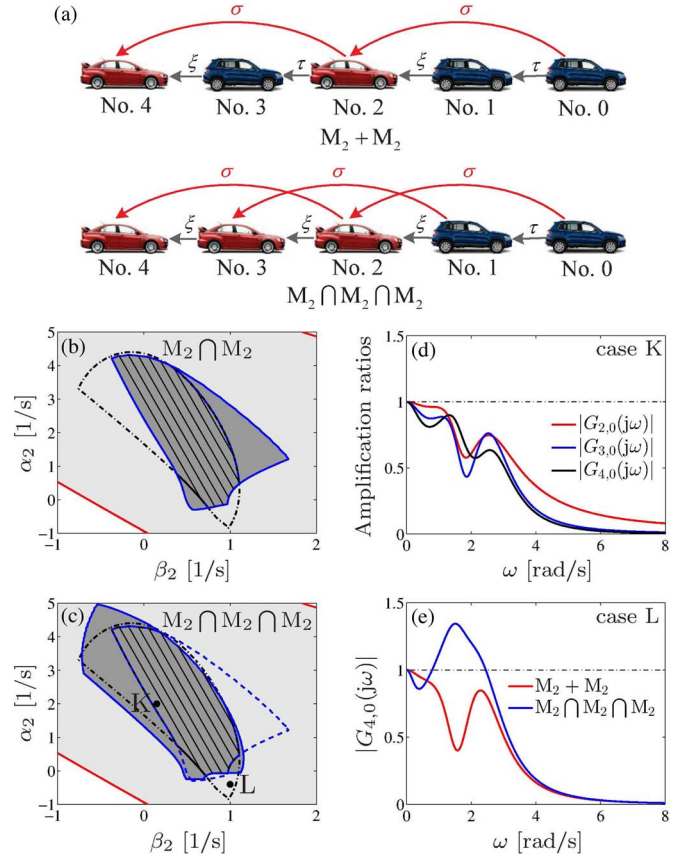


Fig. 12. (a): Networks  $M_2 + M_2$  and  $M_2 \cap M_2 \cap M_2$ . (b,c): Stability diagrams of  $M_2 \cap M_2$  and  $M_2 \cap M_2 \cap M_2$  for  $\sigma = 0.2$  [s]. The solid blue curves represent stability boundaries for  $M_2 \cap M_2$  and  $M_2 \cap M_2 \cap M_2$  while the black dashed-dotted curve denotes the stability boundary of  $M_2$ . For comparison, the stability boundary of  $M_2 \cap M_2$  is reproduced in panel (c) using dashed blue curve. Shading has the same meaning as in Fig. 6(a) while the “\” line-shaded domain highlights where all CCC vehicles are string stable with respect to vehicle 0. (d,e): Bode plots corresponding to points K and L in (c).

Using (53) in (21)–(25) leads to the stability diagrams in  $(\beta_2, \alpha_2)$ -plane, as shown in the fourth row of Fig. 11. Comparing these stable domains with those of  $M_2$  (enclosed by the black dashed-dotted curve), one may notice that intersecting links deteriorates head-to-tail string stability. Besides head-to-tail string stability, one may also want both CCC vehicles 2 and 3 to be capable of attenuating disturbances with respect to vehicle 0. To achieve this, control gains must be chosen from the overlap between the head-to-tail string stable domain of  $M_2 \cap M_2$  (dark gray region) and that of  $M_2$  (enclosed by the black dashed-dotted curve). Such overlap is shaded by “\” lines in Fig. 12(b) for  $\sigma = 0.2$  [s].

To further investigate the effects of link intersections, we compare the dynamics of  $M_2 + M_2$  and  $M_2 \cap M_2 \cap M_2$ ; see Fig. 12(a). As discussed in Section V-A,  $M_2 + M_2$  and  $M_2$  have the same stable domain. In Fig. 12(c), the dark gray domain enclosed by the solid blue curve shows the head-to-tail string stable domain of  $M_2 \cap M_2 \cap M_2$  for  $\sigma = 0.2$  [s]. The head-to-tail string stable domains of  $M_2 \cap M_2$  and  $M_2 + M_2$  are enclosed by the dashed blue and dashed-dotted black curves, respectively. The “\” line-shaded domain indicates the overlap of these three domains, where all CCC vehicles are string stable with respect to vehicle 0. The Bode plots corresponding to the



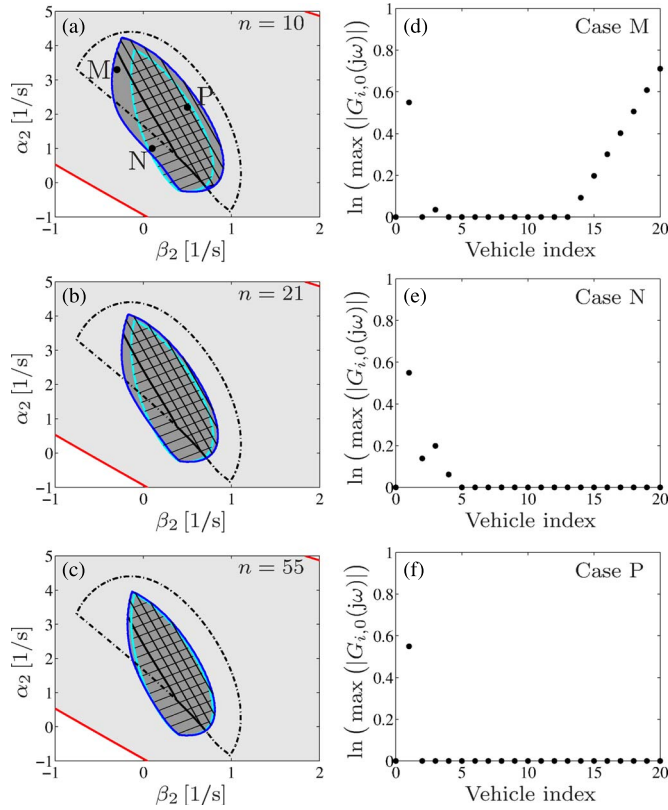


Fig. 13. (a)–(c): Stability diagrams for  $M_2$  intersections of different size as indicated by  $n$ . The black dashed-dotted curve encloses the string stable domain for  $M_2$ . The “\” line-shaded domain is the overlap of the string stable domains for all  $M_2$  intersections of size up to  $n$ . The “/” line-shaded region enclosed by the cyan curve indicates the head-to-tail string stable domain for  $n \rightarrow \infty$ . Other shadings are the same as in Fig. 6(a). (d)–(f): Stability evaluations corresponding to points M–P.

points K and L are shown in Fig. 12(d) and (e), respectively. Panels (c,d) shows that the string stability of CCC vehicles 2–4 can be ensured if control gains are chosen from the “\” line-shaded domain. Panels (c,e) demonstrate that  $M_2 + M_2$  has a larger string stable domain than  $M_2 \cap M_2 \cap M_2$ , even though more CCC vehicles are included in the latter network. This implies that, if the connectivity structure is not appropriately designed, increasing the number of CCC vehicles may deteriorate the performance of a vehicle network.

Repeating the aforementioned process, one can derive stability diagrams for  $M_2$  intersections of any given size, as shown in Fig. 13(a)–(c). As the network size  $n$  increases, the dark gray domain converges to the “/” line-shaded domain (enclosed by the cyan curve), which indicates the head-to-tail stable domain as  $n \rightarrow \infty$  and can be obtained by substituting  $T_1(s) = T_{2,1}(s)$  and  $T_2(s) = T_{2,0}(s)$  into ((29), (30)). The “\” line-shaded domain is the overlap of string stable domains for all  $M_2$  intersections of size up to  $n$ ; cf. Fig. 12(b) and (c). This domain ensures that all CCC vehicles can attenuate disturbances with respect to the head vehicle.

In Fig. 13(a), points M–P are marked to show the system performance when the control gains are chosen from different domains. To evaluate the string stability of vehicle  $i$ , we use the criterion  $\ln(\max_{\omega \geq 0}(|G_{i,0}(j\omega)|)) = 0$  (cf. (23)) and show corresponding results in Fig. 13(d)–(f). Note that the human-driven

vehicle 1 is always string unstable due to  $\tau > \xi_{cr}$ ; cf. (49). One can observe that the control gains from the dark gray domain (case M) only ensure the string stability of vehicle 10 but the disturbance is amplified for larger network size, as shown in Fig. 13(d). When control gains are chosen from the “/” line-shaded domain (case N), it can eliminate the disturbances as  $n \rightarrow \infty$  although some vehicles at the front amplify the disturbances, as shown in Fig. 13(e). Control gains in the cross-shaded domain, which is the overlap between the “\” line-shaded and the “/” line-shaded domains (case P), ensure the string stability of all CCC vehicles, as shown in Fig. 13(f). We remark that this cross-shaded domain does not significantly change with the network size.

When designing  $M_2$  intersections, control gains should be chosen from the cross-shaded domain, which is smaller than the stable domain for  $M_2$  cascades (enclosed by the black dashed-dotted curve). Moreover, in terms of the same network size, the cascade network uses less CCC vehicles than the intersection network. This implies that the intersection of communication links may deteriorate performance of CVSSs.

## VI. CONCLUSION

In this paper, we investigated the effects of heterogeneous connectivity structures and information delays on the longitudinal dynamics of connected vehicle systems (CVSSs). We considered the scenario when vehicles equipped with connected cruise control (CCC) are mixed into the flow of non-CCC vehicles. A framework was presented for CCC design that incorporated information delays, allowed a large variety of connectivity structures, and ensured the existence of a unique equilibrium that was independent of network size, connectivity structure, information delays and control gains. A systematic and efficient method was developed to characterize the system-level performance of CVSSs, which included the calculation of the head-to-tail transfer function that was used to evaluate plant stability and head-to-tail string stability. We also derived stability conditions for large CVSSs with repetitive structures.

Then, a motif-based approach was presented to achieve modular and scalable design of CVSSs. The dynamics of fundamental motifs and the effects of motif combinations were summarized using stability diagrams drawn in the plane of control gains for different values of information delays. The results indicated that when the communication delays are below a threshold, the stability of traffic flow can be improved by increasing the penetration of CCC vehicles and the number of communication links. However, we also demonstrated that if inappropriate control gains or inappropriate connectivity structures were used, increasing the penetration of CCC vehicles might deteriorate the system performance.

The analysis in this paper was based on linearized models that governed the dynamics in the vicinity of equilibrium. In future, we will investigate how the nonlinear dynamics affect the performance of CVSSs. Moreover, to demonstrate the applicability of the motif-based approach while simplifying the computation, we assumed that parameters of human drivers were uniform and constant. However, in reality they may be different across the population and also vary in time. Thus, to

implement CCC in real traffic, further research is needed to study the robustness of CVSs against uncertainties of human parameters. Finally, although the stability of CVSs is related to safety, it does not necessarily ensure collision avoidance. Thus, we plan to extend this work by including safety considerations in the design.

#### APPENDIX A

##### CALCULATING HEAD-TO-TAIL TRANSFER FUNCTION

To demonstrate the applications of (17) and (19), we consider the (4+1)-vehicle network in Fig. 3 as an example, where the coupling matrix is given by

$$\mathbf{T}(s) = \begin{bmatrix} 0 & 0 & 0 & 0 & 0 \\ T_{1,0}(s) & 0 & 0 & 0 & 0 \\ T_{2,0}(s) & T_{2,1}(s) & 0 & 0 & 0 \\ 0 & 0 & T_{3,2}(s) & 0 & 0 \\ 0 & T_{4,1}(s) & T_{4,2}(s) & T_{4,3}(s) & 0 \end{bmatrix}. \quad (54)$$

Applying (17) yields the HTTF

$$G_{4,0}(s) = T_{4,1}(s)T_{1,0}(s) + (T_{4,2}(s) + T_{4,3}(s)T_{3,2}(s)) \times (T_{2,0}(s) + T_{2,1}(s)T_{1,0}(s)) \quad (55)$$

which can be also obtained by utilizing (19) and the modified coupling matrix

$$\hat{\mathbf{T}}(s) = \begin{bmatrix} T_{1,0}(s) & 1 & 0 & 0 \\ T_{2,0}(s) & T_{2,1}(s) & 1 & 0 \\ 0 & 0 & T_{3,2}(s) & 1 \\ 0 & T_{4,1}(s) & T_{4,2}(s) & T_{4,3}(s) \end{bmatrix}. \quad (56)$$

#### APPENDIX B

##### EXPRESSIONS FOR $P_1$ , $P_2$ , $Q_1$ , $Q_2$ , AND $\Delta$ IN (41)

The corresponding quantities are provided as follows.

$$\begin{aligned} P_1 &= \frac{2V'(h^*)}{n} \cdot \text{Re} \left[ \left( j\beta_1\omega_{cr} + \varphi_1 e^{j\omega_{cr}(\sigma-\xi)} \right) (T_h(j\omega_{cr}))^{n-1} \right] \\ &+ 2\omega_{cr}^3 \sin(\omega_{cr}\sigma) + \frac{2V'(h^*)}{n} \omega_{cr}^2 \cos(\omega_{cr}\sigma) \\ &+ 2\omega_{cr} \left( \frac{V'(h^*)\kappa_1}{n} - \varphi_1 \right) \sin(\omega_{cr}(\sigma - \xi)) \\ &- 2 \left( \frac{V'(h^*)\varphi_1}{n} + \kappa_1\omega_{cr}^2 \right) \cos(\omega_{cr}(\sigma - \xi)) \\ P_2 &= 2\omega_{cr} \cdot \text{Im} \left[ \left( j\beta_1\omega_{cr} + \varphi_1 e^{j\omega_{cr}(\sigma-\xi)} \right) (T_h(j\omega_{cr}))^{n-1} \right] \\ &+ 2\omega_{cr}^3 \sin(\omega_{cr}\sigma) - 2\varphi_1\omega_{cr} \sin(\omega_{cr}(\sigma - \xi)) \\ &- 2\kappa_1\omega_{cr}^2 \cos(\omega_{cr}(\sigma - \xi)) \end{aligned} \quad (57)$$

$$\begin{aligned} Q_1 &= \frac{\omega_{cr}^2 W' - 2\omega_{cr} W}{2\omega_{cr} P_2 - \omega_{cr}^2 P_2'}, \quad Q_2 = \frac{\omega_{cr}^2 P_1' - 2\omega_{cr} P_1}{2\omega_{cr} P_2 - \omega_{cr}^2 P_2'} \\ \Delta &= (-2\omega_{cr}^2 Q_1 + P_1 + P_2 Q_2)^2 + 4\omega_{cr}^2 (1 + 2Q_2)(W + P_2 Q_1) \end{aligned} \quad (58)$$

where the prime denotes the derivative with respect to  $\omega_{cr}$  and

$$W = \left| j\beta_1\omega_{cr} + \varphi_1 e^{j\omega_{cr}(\sigma-\xi)} \right|^2 |T_h(j\omega_{cr})|^{2(n-1)} - \left| (j\kappa_1\omega_{cr} + \varphi_1) e^{j\omega_{cr}(\sigma-\xi)} - \omega_{cr}^2 e^{j\omega_{cr}\sigma} \right|^2. \quad (59)$$

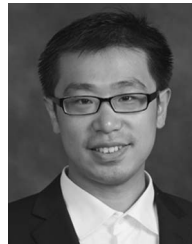
In (57)–(59), the transfer function  $T_h(j\omega_{cr})$  is given in (35).

#### REFERENCES

- [1] D. Helbing, "Traffic and related self-driven many-particle systems," *Rev. Mod. Phys.*, vol. 73, no. 4, pp. 1067–1141, Dec. 2001.
- [2] B. Kerner, *The Physics of Traffic: Empirical Freeway Pattern Features, Engineering Applications, and Theory*. Berlin, Germany: Springer-Verlag, 2004.
- [3] G. Orosz, R. E. Wilson, and G. Stépán, "Traffic jams: Dynamics and control," *Philos. Trans. Roy. Soc. London A, Math. Phys. Sci.*, vol. 368, no. 1928, pp. 4455–4479, Sep. 2010.
- [4] D. Caveney, "Cooperative vehicular safety applications," *IEEE Control Syst.*, vol. 30, no. 4, pp. 38–53, Aug. 2010.
- [5] X. Xiang, W. Qin, and B. Xiang, "Research on a DSRC-based rear-end collision warning model," *IEEE Trans. Intell. Transp. Syst.*, vol. 15, no. 3, pp. 1054–1065, Jun. 2014.
- [6] S. E. Shladover, D. Su, and X.-Y. Lu, "Impacts of cooperative adaptive cruise control on freeway traffic flow," *Transp. Res. Rec., J. Transp. Res. Board*, vol. 2324, pp. 63–70, 2012.
- [7] S. I. Guler, M. Menendez, and L. Meier, "Using connected vehicle technology to improve the efficiency of intersections," *Transp. Res. C, Emerging Technol.*, vol. 46, pp. 121–131, Sep. 2014.
- [8] S. S. Avedisov and G. Orosz, "Nonlinear network modes in cyclic systems with applications to connected vehicles," *J. Nonlinear Sci.*, vol. 25, no. 4, pp. 1015–1049, Aug. 2015.
- [9] C. Suthaputthakun, Z. Sun, and M. Dianati, "Applications of vehicular communications for reducing fuel consumption and CO<sub>2</sub> emission: The state of the art and research challenges," *IEEE Commun. Mag.*, vol. 50, no. 12, pp. 108–115, Dec. 2012.
- [10] T. Robinson, E. Chan, and E. Coelingh, "Operating platoons on public motorways: An introduction to the SARTRE platooning programme," in *Proc. 17th World Congr. Intell. Transp. Syst.*, 2010, pp. 1–11.
- [11] G. J. L. Naus, R. P. A. Vugts, J. Ploeg, M. J. G. van de Molengraft, and M. Steinbuch, "String-stable CACC design and experimental validation: A frequency-domain approach," *IEEE Trans. Veh. Technol.*, vol. 59, no. 9, pp. 4268–4279, Nov. 2010.
- [12] R. Kianfar *et al.*, "Design and experimental validation of a cooperative driving system in the grand cooperative driving challenge," *IEEE Trans. Intell. Transp. Syst.*, vol. 13, no. 3, pp. 994–1007, Sep. 2012.
- [13] A. Geiger *et al.*, "Team AnnieWAY's entry to the 2011 grand cooperative driving challenge," *IEEE Trans. Intell. Transp. Syst.*, vol. 13, no. 3, pp. 1008–1017, Sep. 2012.
- [14] A. Alam, J. Mårtensson, and K. H. Johansson, "Experimental evaluation of decentralized cooperative cruise control for heavy-duty vehicle platooning," *Control Eng. Pract.*, vol. 38, pp. 11–25, May 2015.
- [15] M. di Bernardo, A. Salvi, and S. Santini, "Distributed consensus strategy for platooning of vehicles in the presence of time-varying heterogeneous communication delays," *IEEE Trans. Intell. Transp. Syst.*, vol. 16, no. 1, pp. 102–112, Feb. 2015.
- [16] L. Zhang and G. Orosz, "Designing network motifs in connected vehicle systems: Delay effects and stability," presented at the Proc. ASME Dynamic Systems Control Conf., 2013, Paper DSCC2013-4081.
- [17] J. I. Ge and G. Orosz, "Dynamics of connected vehicle systems with delayed acceleration feedback," *Transp. Res. C, Emerging Technol.*, vol. 46, pp. 46–64, Sep. 2014.
- [18] W. B. Qin, M. M. Gomez, and G. Orosz, "Stability and frequency response under stochastic communication delays with applications to connected cruise control design," *IEEE Trans. Intell. Transp. Syst.*, submitted for publication.
- [19] U. Alon, *An Introduction to Systems Biology: Design Principles of Biological Circuits*. Boca Raton, FL, USA: CRC Press, 2007.
- [20] A. G. Ulsoy, H. Peng, and M. Çakmakci, *Automotive Control Systems*. Cambridge, U.K.: Cambridge Univ. Press, 2012.



- [21] G. Orosz, "Connected cruise control: Modeling, delay effects, and nonlinear behavior," *Veh. Syst. Dyn.*, submitted for publication.
- [22] D. Swaroop and J. K. Hedrick, "String stability of interconnected systems," *IEEE Trans. Autom. Control*, vol. 41, no. 3, pp. 349–357, Mar. 1996.
- [23] P. Seiler, A. Pant, and K. Hedrick, "Disturbance propagation in vehicle strings," *IEEE Trans. Autom. Control*, vol. 49, no. 10, pp. 1835–1842, Oct. 2004.
- [24] K. H. Rosen, *Discrete Mathematics and its Applications*, 7th ed. New York, NY, USA: McGraw-Hill, 2012.
- [25] T. Insperger and G. Stépán, *Semi-Discretization for Time-Delay Systems*. New York, NY, USA: Springer-Verlag, 2011.
- [26] C. A. Rabbath and N. Léchervin, *Discrete-Time Control System Design With Applications*. New York, NY, USA: Springer-Verlag, 2014.
- [27] F. Bai and H. Krishnan, "Reliability analysis of DSRC wireless communication for vehicle safety applications," in *Proc. IEEE Intell. Transp. Syst. Conf.*, 2006, pp. 355–362.
- [28] W. B. Qin, M. M. Gomez, and G. Orosz, "Stability analysis of connected cruise control with stochastic delays," in *Proc. Amer. Control Conf.*, 2014, pp. 5534–5539.
- [29] P. Wagner, "Fluid-dynamical and microscopic description of traffic flow: A data-driven comparison," *Philos. Trans. Roy. Soc. London A, Math. Phys. Sci.*, vol. 368, no. 1928, pp. 4481–4495, Sep. 2010.
- [30] K. Engelborghs, T. Luzyanina, and G. Samaey, "DDE-biftool v. 2.00: A Matlab Package for Bifurcation Analysis of Delay Differential Equations," Dept. Comput. Sci., Katholieke Univ. Leuven, Leuven, Belgium, Tech. Rep. TW-330, 2001.



**Linjun Zhang** received the B.Eng. degree in automation from Northeastern University, Shenyang, China, in 2005 and the M.Eng. degree in control science and engineering from Beijing University of Aeronautics and Astronautics, Beijing, China, in 2009. He is currently working toward the Ph.D. degree in mechanical engineering at University of Michigan, Ann Arbor, MI, USA. His research interests include intelligent transportation systems, vehicle dynamics and control, nonlinear control, time-delay systems, complex networks, and system identification.



**Gábor Orosz** received the M.Sc. degree in engineering physics from Budapest University of Technology, Budapest, Hungary, in 2002 and the Ph.D. degree in engineering mathematics from University of Bristol, Bristol, U.K., in 2006. He held postdoctoral positions with University of Exeter, Devon, U.K., and University of California, Santa Barbara, CA, USA, before joining University of Michigan, Ann Arbor, MI, USA, in 2010 as an Assistant Professor of mechanical engineering. His research focuses on nonlinear dynamics and control, time-delay systems,

and networks and complex systems, with applications on connected and automated vehicles and biological networks.